nanomaterials

MDPI

Article

Systematic Microwave-Assisted Postsynthesis of Mn-Doped Cesium Lead Halide Perovskites with Improved Color-Tunable Luminescence and Stability

Yaheng Zhang [1], Chao Fan [1], Jianghong Tang [1], Gaoming Huang [1], Xinfa Qiang [2], Yu Fu [1], Wenjuan Zhou [1], Juan Wu [1] and Shouqiang Huang [1,*]

[1] Jiangsu Key Laboratory of E-Waste Recycling, School of Chemistry and Environmental Engineering, Jiangsu University of Technology, Changzhou 213001, China; zhangyaheng@jsut.edu.cn (Y.Z.); chaofan19930703@163.com (C.F.); tjh01@jsut.edu.cn (J.T.); hanggaoming1122@163.com (G.H.); fuyu@jsut.edu.cn (Y.F.); 2019560060@jsut.edu.cn (W.Z.); jintanwujuan@163.com (J.W.)

[2] Jiangsu Key Laboratory of Advanced Structural Materials and Application Technology, Nanjing Institute of Technology, Nanjing 211167, China; qiangxinfa@163.com

* Correspondence: hshouqiang@126.com

Abstract: The metal doping at the Pb^{2+} position provides improved luminescence performance for the cesium lead halide perovskites, and their fabrication methods assisted by microwave have attracted considerable attention due to the advantages of fast heating and low energy consumption. However, the postsynthetic doping strategy of the metal-doped perovskites driven by microwave heating still lacks systematic research. In this study, the assembly of $CsPbBr_3/CsPb_2Br_5$ with a strong fluorescence peak at 523 nm is used as the $CsPbBr_3$ precursor, and through the optimization of the postsynthetic conditions such as reaction temperatures, Mn^{2+}/Pb^{2+} feeding ratios, and Mn^{2+} sources, the optimum Mn^{2+}-doped product ($CsPb(Cl/Br)_3$:Mn) is achieved. The exciton fluorescence peak of $CsPb(Cl/Br)_3$:Mn is blueshifted to 437 nm, and an obvious fluorescence peak attributing to the doped Mn^{2+} ions at 597 nm is obtained. Both the $CsPbBr_3$ precursor and $CsPb(Cl/Br)_3$:Mn have high PLQY and stability because there are $CsPb_2Br_5$ microcubic crystals to well disperse and embed the $CsPbBr_3$ nanocrystals (NCs) in the precursor, and after Mn^{2+}-doping, this structure is maintained to form $CsPb(Cl/Br)_3$:Mn NCs on the surface of their microcrystals. The exploration of preparation parameters in the microwave-assisted method provides insights into the enhanced color-tunable luminescence of the metal-doped perovskite materials.

Keywords: microwave heating; postsynthetic doping strategy; Mn^{2+}-doped cesium lead halide perovskite; photoluminescence; stability

Citation: Zhang, Y.; Fan, C.; Tang, J.; Huang, G.; Qiang, X.; Fu, Y.; Zhou, W.; Wu, J.; Huang, S. Systematic Microwave-Assisted Postsynthesis of Mn-Doped Cesium Lead Halide Perovskites with Improved Color-Tunable Luminescence and Stability. *Nanomaterials* **2022**, *12*, 2535. https://doi.org/10.3390/nano12152535

Academic Editor: Julia Pérez-Prieto

Received: 28 April 2022
Accepted: 20 July 2022
Published: 23 July 2022

1. Introduction

Perovskite solar cells were rated as one of the "Top Ten Scientific Breakthroughs" by Science in 2013, leading to the emergence of the "perovskite craze" in the world. However, its key core material, organic-inorganic hybrid perovskite, has poor stability, and it is easy to degrade in a short time under the condition of exposure to light, heat, water, or oxygen, which is seriously restricted its popularization and application [1,2]. In this context, people began to pay attention to all-inorganic trihalogen perovskite materials (e.g., $CsPbBr_3$), which have similar excellent photoelectric performance and better stability. Since the first report of all-inorganic perovskite nanocrystalline materials in January 2015 [3], $CsPbX_3$ (X = Cl, Br, I, or their mixture) nanocrystals (NCs) have attracted much attention due to their core advantages such as excellent photoelectric properties, broad application prospects and simple preparation process [4–7]. Related research has mushroomed and shown a rapid growth trend, which has become a new research frontier in the field of photoelectric materials. However, the extensive use of toxic Pb^{2+} in perovskite NCs seriously limits their

practical application. At the same time, $CsPbX_3$ also faces the urgent need to adjust or improve its performance, especially luminescence performance, to adapt to its photoelectric application or expand its application scope.

There are Cs^+, X^- and Pb^{2+} in $CsPbX_3$ lattice. Researches show that compared with X^- and Pb^{2+}, there is little influence on its luminescence properties by doping other ions at Cs^+ [8,9]. By doping different halogen ions to the position of X^-, the band gap could be changed, and the luminescence peaks of $CsPbX_3$ can be regulated to some extent [3,10]. The 6s and 6p orbitals of Pb^{2+} contribute greatly to the formation of valence band top and conduction band bottom, and the lattice position of Pb^{2+} plays an extremely important role in determining its photoelectric properties [11]. Accordingly, it is desirable to conduct effective metal ion doping at the Pb^{2+} position [12]. That is, the dopants replace part of Pb^{2+} ions rather than adsorbing on the surface of the NCs. Mn^{2+} is one of the most popular dopants. The main reasons are as follows: firstly, Mn^{2+} has the same charge number as Pb^{2+} and a smaller ionic radius, which is conducive to doping [13–17]; Secondly, Mn^{2+} can be used as a tracer ion [14,18]. The successful doping and doping site can be judged by its emission or electron paramagnetic resonance spectra [19,20]. Moreover, its stokes displacement is large, and its self-absorption effect is small. Mn^{2+} is also an exciton coupling agent, which can obtain energy from the matrix (known as host) to exhibit its characteristic luminescence [21,22]. The driving force is another important factor affecting effective doping. The doping driving force has at least two functions: one is to interrupt part of the Pb-X bonds in the $CsPbX_3$ lattice, and the other is to promote the diffusion of dopants, such as Mn^{2+} ions, and eventually occupy part of the Pb^{2+} sites. At present, hot injection is the most common doping method in preparation of $CsPbX_3$ NCs [23–25]. In addition, microwave, ultrasound or pressure can also drive impurity ions into $CsPbX_3$ lattice [26,27]. Among various synthesis methods, the microwave-assisted method has attracted much attention, wherein microwave radiation is used as a relatively fast energy input source to drive the reaction. Compared with other heating methods, microwave heating has the advantages of more uniform, fast reaction, low energy consumption and selective heating, which are conducive to the nucleation of $CsPbX_3$ NCs.

There are two main doping strategies at the lattice site of Pb^{2+}: in situ doping and postsynthetic doping. The former is the addition of dopants, Cs^+ and Pb^{2+} sources into the reaction system [28–30], belonging to nucleation doping. The latter is based on the dopant and the pre-prepared $CsPbX_3$ NCs as the starting materials, and the doped $CsPbX_3$ NCs are obtained after this post-treatment [31,32] belonging to growth doping. The process of nucleation doping to form $CsPbCl_3$:Mn^{2+} NCs under thermal driving is fast, completed in about 5 s, and the postsynthetic doping strategy to form $CsPbCl_3$:Mn^{2+} NCs is slow but easy to control [33]. At present, most of $CsPbX_3$:M^{Z+} (M^{Z+} represents the doped metal ions) NCs are synthesized by in situ doping [12,23,24,28,29]. It was also reported that $CsPbX_3$: M^{Z+} NCs can also be prepared by a postsynthetic doping strategy. For example, Donegá et al. [31] synthesized $CsPbBr_3$:M^{2+} NCs by mixing MBr_2 (M = Zn^{2+}, Cd^{2+}, Sn^{2+}) and the benzene dispersion of $CsPbBr_3$ NCs at room temperature. Xu et al. [33] found that $CsPbCl_3$:Mn^{2+} NCs could be formed by mixing $MnCl_2$ dispersion (dispersed in 1-octadecene (ODE)), oleylamine (OLA), and oleic acid (OA) with $CsPbCl_3$ nanocrystals at 150 °C and stirring. Wang et al. [32] reported that Mn^{2+}-doped NCs could be obtained by mixing the N, N-dimethylformamide dispersion of $MnCl_2$ with the benzene dispersion of $CsPbBr_3$ NCs at 20 °C and stirring violently. Xia et al. [34] mixed and stirred the hexane dispersion of $CsPbBr_3$ and $CsPbCl_3$:Mn^{2+} NCs at room temperature to obtain $CsPb(Cl, Br)_3$:Mn^{2+} NCs. In the application of microwave heating, Liu et al. [26] put the reaction mixture, which included cesium acetate, $PbCl_2$, $MnCl_2$, ODE, bis(2,4,4trimethylpentyl) phosphinic acid (TMPPA), and OLA into a microwave oven, and $CsPbCl_3$:Mn^{2+} was obtained after 20 min reaction at 800 W by this one-step microwave-assisted preparation method. The maximum photoluminescence quantum yield (PLQY) belongs to the $CsPb_{0.79}Mn_{0.21}Cl_3$ NCs with a value of 26%. Yang et al. [35] synthesized $CsPb(Br,Cl)_3$:Mn^{2+} NCs without inert atmosphere at room temperature by a microwave-assisted method, which is also attributed to the in

situ doping method. However, it is noted that, the systematic research on postsynthetic doping of Mn^{2+} into $CsPbX_3$ NCs driven by microwave is still very limited, which needs further investigation.

In this study, the assembly of $CsPbBr_3/CsPb_2Br_5$ with excellent luminescent properties was initially obtained by screening the synthesis conditions under microwave-driven reactions, and the optimum assembly was used as the $CsPbBr_3$ precursor. In comparison with a domestic microwave oven, the reaction temperature and pressure of the mixture can be controlled automatically in a closed reaction bottle with high safety. On the basis of the $CsPbBr_3$ precursor, the Mn-doped lead halide perovskites with excellent luminescence were obtained by investigating the reaction temperatures, times, Mn^{2+} doping ratios, Mn^{2+} sources, and the volume ratios of ODE/diethylene glycol butyl ether (DGBE). The structure and PL emission spectra of the Mn^{2+} doped products are investigated to obtain the best condition. From the comparison between the $CsPbBr_3$ precursor and the optimum Mn^{2+} doped product in PL emission, morphology, composition, and stability, the mechanism for the improved PL quantum yields (PLQYs) and stabilities are discussed. Under UV excitation, the Mn^{2+} doped products not only exhibit the exciton luminescence of perovskite (also known as band edge luminescence) but also the luminescence of Mn^{2+} ions, realizing the tunable luminescence color.

2. Materials and Methods

2.1. Chemicals and Materials

Cs_2CO_3 (cesium carbonate, 99.9%), $PbBr_2$ (lead bromide, 99.0%), ODE (90%), OA (90%), OLA (90%), DGBE (99.0%), $MnCl_2{\cdot}4H_2O$ (manganese chloride tetrahydrate, 99.0%), $MnBr_2{\cdot}4H_2O$ (manganese bromide hydrate, 98.0%), $MnSO_4{\cdot}H_2O$ (manganese sulfate monohydrate, 99.0%), $C_4H_6MnO_4{\cdot}4H_2O$ (manganese acetate tetrahydrate, 99.0%), and $C_{10}H_{14}MnO_4$ (manganese acetylacetonate, 99.5%) were purchased from Shanghai Makclin Biochemical Co., Ltd. (Shanghai, China). Cyclohexane (99.7%) and ethyl acetate (99.5%) were purchased from China National Pharmaceutical Group Corporation (Beijing, China).

2.2. Preparation of the $CsPbBr_3$ Precursor

Firstly, Cs_2CO_3 (0.0326 g), $PbBr_2$ (0.1668 g), DGBE (5.00 mL), ODE (5.00 mL), OA (0.50 mL), and OLA (0.50 mL) were put into the microwave flask. Then, the stirrer was added, and put the microwave flask into the microwave instrument (NOVA-2S, China). The pristine $CsPbBr_3$ was synthesized by temperature programming (heating from room temperature to 150 °C for 3 min and holding for 15 min). When the samples were cooled to 71 °C, the microwave flasks were taken out from the microwave instrument. After cooling to room temperature with ice water, the mixtures were centrifuged at 8500 rpm/min for 8 min, and then the solids were washed twice with ethyl acetate (centrifugation). All the obtained $CsPbBr_3$ precipitates were temporarily placed in the centrifuge tube. To find the optimum condition, other kinds of $CsPbBr_3$ were also prepared with different mole ratios of $Cs_2CO_3/PbBr_2$ (0.1/0.25~0.1/0.5), temperatures (100~200 °C), and volume ratios of ODE/DGBE (5/2.5~5/12.5).

2.3. Postsynthesis of Mn^{2+} Doped Perovskites

DGBE, ODE (5 mL), OA (0.50 mL), OLA (0.50 mL), and $MnCl_2{\cdot}4H_2O$ (0.90 mmol) were added into the above centrifuge tube containing the $CsPbBr_3$ precursor. After the mixture was uniformly dispersed, it was transferred to the microwave flask. The stirrer was added to the flask, which was then put into the microwave instrument for reaction. The process is the same as that mentioned above with different temperatures, times, Mn^{2+} doping ratios, and volume ratios of ODE/DGBE. Finally, the products were cooled with ice water, centrifuged at 8500 rpm/min for 8 min, and washed twice with ethyl acetate, which was then stored in cyclohexane. Meanwhile, other Mn^{2+} sources of $MnBr_2{\cdot}4H_2O$, $MnSO_4{\cdot}H_2O$, $C_4H_6MnO_4{\cdot}4H_2O$, and $C_{10}H_{14}MnO_4$ were also chosen to substitute $MnCl_2{\cdot}4H_2O$ to prepare the products for comparison.

2.4. Characterizations

The PL spectra, PLQYs, and stability measurements of the $CsPbBr_3$ precursor and Mn^{2+}-doped products cyclohexane solutions (all the optical absorbances were adjusted to the same before detection) were tested by using a fluorescence spectrophotometer (FluoroMax Plus, Horiba Scientific), and the excitation wavelength was 365 nm. For the test of PLQY, an integrating sphere accessory was used, and the parameters of 2.4 nm slit width and 1s integration time were used; the excitation wavelength was 365 nm, and the scanning range of emission spectrum was 415–710 nm; cyclohexane was taken as a blank sample, the product concentration was adjusted to make the absorbance value ≤ 0.05; the PLQY calculations were performed using the Horiba Scientific FluorEssence software, and the integrating sphere calibration file was selected in the software; the sample spectrum and blank spectrum were imported respectively, and the fitting ranges of excitation and emission wavelengths were adjusted to obtain the PLQY value. The PL decay curves were recorded on the same fluorescence spectrophotometer, where a 370 nm NanoLED pulsed source was used as the excitation source. The UV-vis absorption spectra were detected on a UV1800PC spectrophotometer (Shanghai Jinghua Instruments, Room 1310, Building 4, Songjiang Wanda Plaza, Shanghai, China). The X-ray diffraction (XRD) investigations were performed using a Philips X'Pert Powder Diffractometer system with Cu K_α radiation. The morphologies and compositions were recorded by the Zeiss Sigma 500 field emission scanning electron microscope (SEM) and the JEOL JEM 2100F transmission electron microscope (TEM). The surface compositions of the samples were obtained by the K-Alpha + X-ray photoelectron spectroscopy system (XPS, Thermo Fisher Scientific, Building 3& 6& 7, 27 Xinjinqiao Road, Pudong New Area, Shanghai, China). Electron paramagnetic resonance (EPR) was measured on a Bruker A300 spectrometer. Fourier transform infrared (FTIR) spectra were recorded on a Nicolet 6700 spectrometer.

3. Results and Discussion

3.1. Optimization of the Synthesis of the $CsPbBr_3$ Precursor

The pristine $CsPbBr_3$ products are first prepared by a microwave method, wherein the feed mole ratios of $Cs_2CO_3/PbBr_2$, temperatures of microwave reaction, and the volume ratios of ODE/DGBE added are discussed to obtain products with better luminous performance. As shown in Figure S1, when the mole ratio of $Cs_2CO_3/PbBr_2$ is 0.1/0.45, the product shows excellent PL emission intensity, indicating a suitable feed ratio is one of the important factors for obtaining optimum products. The reaction temperatures vary from 100 to 200 °C, and the highest PL intensity is exhibited at 150 °C (Figure S2). To absorb microwaves better and achieve a higher microwave reaction effect, the polar substance content of DGBE in the system needs to be concerned. In the experiments, the addition of ODE is constant, while the volume ratios of ODE/DGBE are changed. When the ratio reaches 5/5, the product has the strongest PL emission (Figure S3). On the basis of the above optimized parameters, the best product is obtained under the conditions of $Cs_2CO_3/PbBr_2$ = 0.1/0.45, temperature of 150 °C, and ODE/DGBE = 5/5.

Figure 1a shows the XRD pattern of the best product. It can be found that most of the diffraction peaks are consistent with the standard card of PDF#54-0751, which belongs to the monoclinic phase of $CsPbBr_3$, and the 2θ at 21.55° and 30.84° correspond to the (010) and (002) crystal planes of $CsPbBr_3$, respectively. In addition, there are also diffraction peaks assigned to the standard card of PDF#54-0753, indicating that there is a small amount of $CsPb_2Br_5$ in the pristine $CsPbBr_3$ product. The obvious diffraction peaks indicate their suitable crystallinity. Figure 1b shows the PL emission spectrum of the pristine $CsPbBr_3$ excited at 365 nm, and a narrow, strong fluorescence emission peak at 523 nm with 18 nm half-peak width (FWHM) is present. Figure 1c shows the UV-vis absorption spectrum of the pristine $CsPbBr_3$, and the first excitonic absorption peak is located at 515 nm. The photographs of the pristine $CsPbBr_3$ respectively excited under natural and 365 nm UV light are given in Figure 1d, and a bright green color is exhibited with a high PLQY of

about 93%. This assembly of $CsPbBr_3$ containing $CsPb_2Br_5$ is used as the precursor for the synthesis of the Mn^{2+}-doped products.

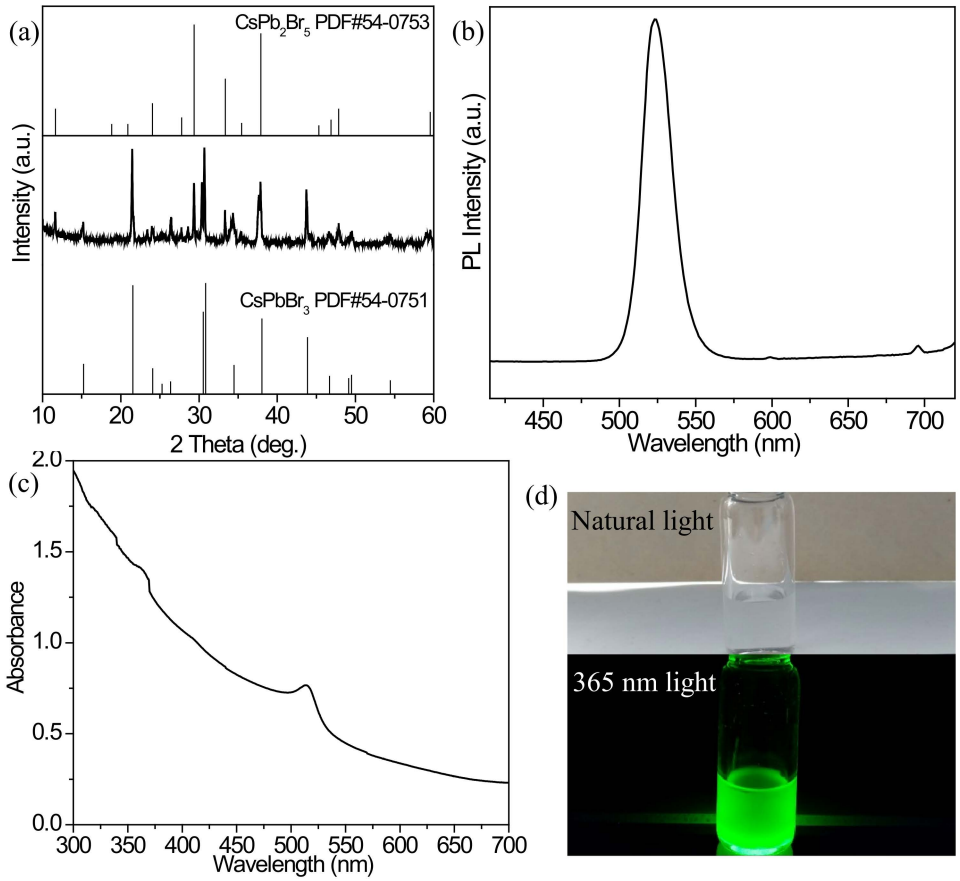

Figure 1. (**a**) XRD pattern, (**b**) PL emission and (**c**) UV-vis absorption spectra of the best pristine $CsPbBr_3$ achieved under the conditions of $Cs_2CO_3/PbBr_2$ = 0.1/0.45, temperature of 150 °C and ODE/DGBE = 5:5. (**d**) Optical images of the cyclohexane solution containing the best pristine $CsPbBr_3$ under the environments of natural and 365 nm light.

3.2. Postsynthesis of the Mn^{2+} Doped Products

3.2.1. Effect of Reaction Temperature

On the basis of the $CsPbBr_3$ precursor with excellent luminescent properties, the Mn^{2+} post-doping experiments are carried out. In a chemical reaction, thermodynamic and kinetic factors determine the reaction rate, yield, and morphology of the products, so the reaction temperature is an important factor for the doping experiments. The doped inorganic perovskites are synthesized by doping Mn^{2+} into the $CsPbBr_3$ precursor, and $MnCl_2{\cdot}4H_2O$ is selected as the Mn^{2+} source. The effect of reaction temperature on the Mn^{2+} doped products is investigated under the Mn^{2+}/Pb^{2+} feed ratio of 1/1, ODE/DGBE volume ratio of 5/5, and reaction time of 15 min. Figure 2a shows the XRD patterns of the products synthesized at different temperatures. In comparison with the standard card PDF#54-0751 of $CsPbBr_3$, the diffraction peaks of the products in this system all shift to higher angles. The reason for this phenomenon is that parts of Pb^{2+} and Br^- in the $CsPbBr_3$ precursor have been replaced by Mn^{2+} and Cl^-, respectively. Because the ionic radius of Mn^{2+} is smaller than that of Pb^{2+} and the ionic radius of Cl^- is also smaller than that of Br^- [12,32,36], the substitution of this cation and anion causes perovskite lattice shrinkage. As the increase in reaction temperatures, some diffraction peaks are gradually enhanced, such as the peak at $2\theta = 31.5°$, indicating the suitable crystallinity of the Mn^{2+} doped products. Furthermore, the diffraction peaks of $CsPb_2Br_5$ corresponding to PDF#54-0753 almost disappeared even at the lowest temperature of 80 °C, suggesting the products obtained mainly consisted of

the Mn^{2+} doped $CsPbBr_3$. It is noted that, through the replacement of Pb^{2+} in $CsPb_2Br_5$ by Mn^{2+}, the phases of $Cs(Pb/Mn)Br_5$ and $CsMn_2Br_5$ (1:2:5) are difficult to form, but $CsMnBr_3$ (1:1:3) often tends to produce [24,37]. Accordingly, after the partial replacements of Pb^{2+} by Mn^{2+} and Br^- by Cl^-, the 1:2:5 structure is destroyed, and instead, the 1:1:3 structure of $Cs(Mn/Pb)(Cl/Br)_3$ is preferred to generate.

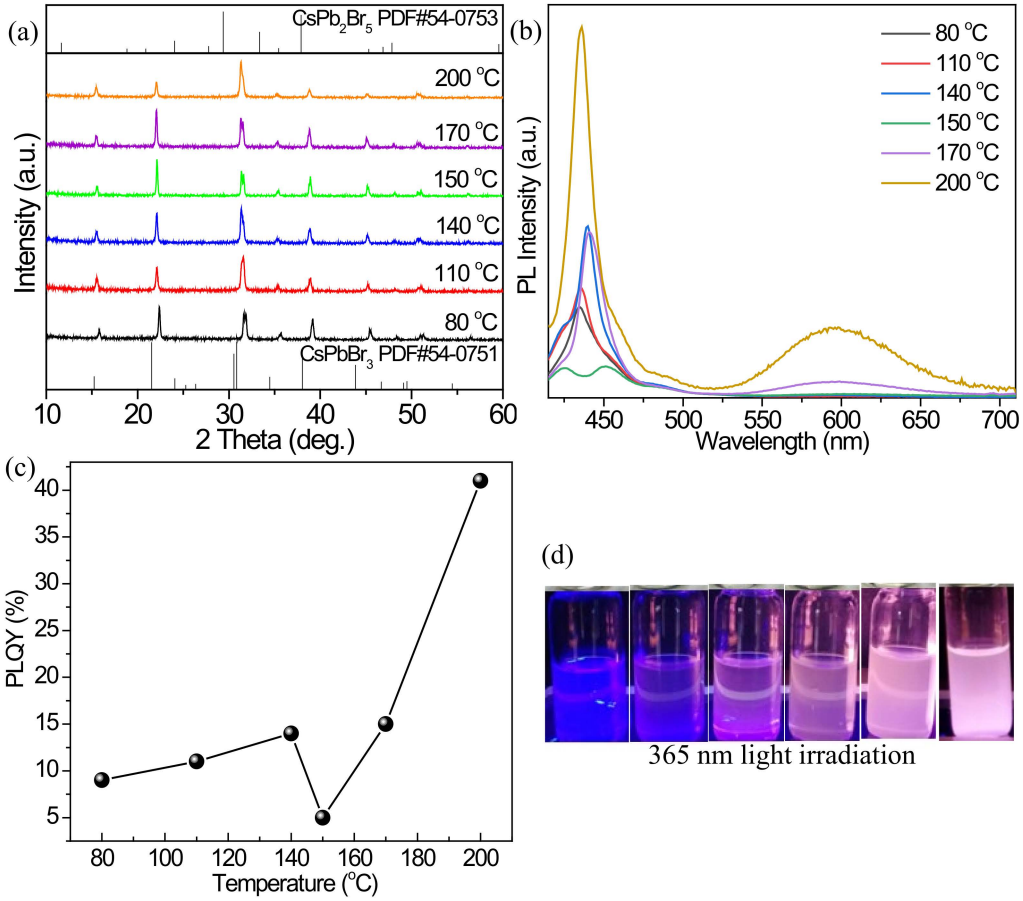

Figure 2. (**a**) XRD patterns, (**b**) PL emission spectra, and (**c**) PLQYs of the Mn^{2+}-doped products fabricated at different reaction temperatures. (**d**) Optical images of the cyclohexane solutions containing the Mn^{2+}-doped products under the environment of 365 nm light: from left to right, the reaction temperatures are 80, 110, 140, 150, 170, and 200 °C, respectively.

Figure 2b is the PL emission spectra of the Mn^{2+} doped products synthesized in the reaction temperature system. Compared with the $CsPbBr_3$ precursor, the exciton emission peaks of the products are blueshifted from 523 nm to about 440 nm (Figure S4a), which is caused by the partial replacement of Br^- ions in the $CsPbBr_3$ precursor by Cl^- ions of $MnCl_2$. At 80 °C, the Cl^- ions have entered the $CsPbBr_3$ precursor, and a large blueshift of the exciton emission peak is present. As the temperature increases from 80 to 140 °C, the exciton fluorescence peak intensity is first enhanced and then decreased, while there is almost no Mn^{2+}-related fluorescence peak. At the higher temperature of 170 °C, an obvious Mn^{2+} characteristic fluorescence emission peak appears near 600 nm (Figure S4b), indicating that Mn^{2+} ions have begun to be doped into the $CsPbBr_3$ precursor. When the reaction temperature reaches 200 °C (the highest temperature of the microwave instrument can reach), the intensity of Mn^{2+} characteristic fluorescence emission peak is the largest, and the exciton energy transfer efficiency from excitons to Mn^{2+} is the highest. At this temperature, the exciton emission peak intensity is also obvious, and the calculated PLQY from both the exciton and Mn^{2+} emission peaks reaches 41% (Figure 2c), which is higher than those obtained at other temperatures, so 200 °C is a suitable reaction temperature for

Mn^{2+} post-doping. Therefore, the Cl^- and Br^- can exchange at a lower temperature in the microwave reaction system, while, for the exchange of Pb^{2+} by Mn^{2+}, it needs a higher temperature. The photographs of the doped products irradiated by natural and 365 nm UV light are given in Figure 2d. When the reaction temperature reaches 200 °C, very bright orange light is emitted from the Mn^{2+} doped product, which is very different from the products prepared at other reaction temperatures, indicating that Mn^{2+} ions have been effectively doped in the $CsPbBr_3$ precursor at this condition.

3.2.2. Effect of Reaction Time

In the growth process of crystals, the reaction time also has a great influence on the luminescence intensity of the samples. For example, if the crystal growth time is too short, the defects caused by incomplete growth would lead to the weakening of the luminescence intensity. In contrast, the long growth time may cause the agglomeration and stacking of crystals to form large particles, affecting the luminescence of the samples. Accordingly, the effect of reaction time on the doped products is investigated under the Mn^{2+} ($MnCl_2{\cdot}4H_2O$)/Pb^{2+} feeding ratio of 1/1, ODE/DGBE volume ratio of 5/5, and reaction temperature of 200 °C.

Figure 3a shows the XRD patterns of the Mn^{2+} doped products synthesized in the reaction time system. The diffraction peaks are generally shifted to higher angles (Figure S5) compared with the standard card PDF#54-0751 of $CsPbBr_3$. The reason is the same as that of the temperature system, which is caused by the lattice shrinkage from the Mn^{2+} substitution. In addition, with the increase in reaction time, the crystallinity of the products seems to be enhanced. The PL spectra in Figure 3b show that the intensities of exciton emission peaks at 436 nm and Mn^{2+} characteristic fluorescence peak at 595 nm gradually decrease with the increase in reaction time, and the PLQY of 41% at 15 min declines to about 19% at 60 min (Figure 3c). It is probably that the crystallization time is too long, and larger particles are formed from $CsPbBr_3$, which is consistent with the XRD results, resulting in the decrease in PLQY. Figure 3d shows the photographs of the Mn^{2+} doped products synthesized at different reaction times. Under 365 nm UV light irradiation, the products at 40 and 50 min emit relatively obvious orange light. As for the 15 min-product, its orange light emission is weaker, which is caused by the large contribution of exciton blue emission.

3.2.3. Effect of Mn^{2+} and Pb^{2+} Feeding Ratio

Different Mn^{2+}/Pb^{2+} feeding ratios also affect the luminescence properties of the Mn^{2+} doped products. Because of the use of $MnCl_2$ as a Mn^{2+} source, Mn^{2+} doping also leads to the exchange of Cl^- and Br^-. To ensure the experiments can be fully performed, the reaction time of 30 min is chosen, while the other conditions of a temperature of 200 °C and ODE/DGBE volume ratio of 1/1 are not changed. Figure 4a shows the XRD patterns of the products synthesized with different Mn^{2+}/Pb^{2+} feeding ratios. Compared with the standard card PDF#54-0751 of $CsPbBr_3$, when the Mn^{2+}/Pb^{2+} feeding ratio is 0.2/1, the introduction of $MnCl_2$ does not cause a significant change in the diffraction peak intensities and positions (Figure S6), and the high crystallinity is maintained. With the increase in Mn^{2+}/Pb^{2+} feeding ratios, the redshifts of the diffraction peaks are present, and the crystallinity of the Mn^{2+} doped products gradually deteriorates with some impurity phases because excessive Mn^{2+} may destroy the $CsPbBr_3$ crystals. The PL emission spectra of the Mn^{2+} doped products are given in Figure 4b. For the product with a feeding ratio of 0.2/1, the exciton fluorescence emission is strongest, but no obvious fluorescence emission of Mn^{2+} can be observed (Figure S7). With the increase in the Mn^{2+}/Pb^{2+} feeding ratio and the introduced Cl^- ions, the blueshifts of the exciton emissions are clearly present, and the highest Mn^{2+} luminescence intensity appears at the ratio of 2/1. When the Mn^{2+}/Pb^{2+} feeding ratio further increases to 3/1, the Mn^{2+} emission peak is largely weakened again, and the exciton emission peak even redshifts, indicating that excessive $MnCl_2$ seriously affects the ion exchanges occur between Mn^{2+} and Pb^{2+} and Cl^- and Br^- in the system, and causes damage to the original perovskite structure. At the Mn^{2+}/Pb^{2+} feeding ratio of

2/1, the highest PLQY of 98% is obtained (Figure 4c), so this Mn^{2+}/Pb^{2+} ratio is a suitable proportion. Figure 4d shows the photographs of the products irradiated by natural and 365 nm UV light. When the Mn^{2+}/Pb^{2+} feeding ratio is 0.2/1, cyan light can be emitted under UV light. As for the product with the optimum feeding ratio of 2/1, the visible orange light is emitted.

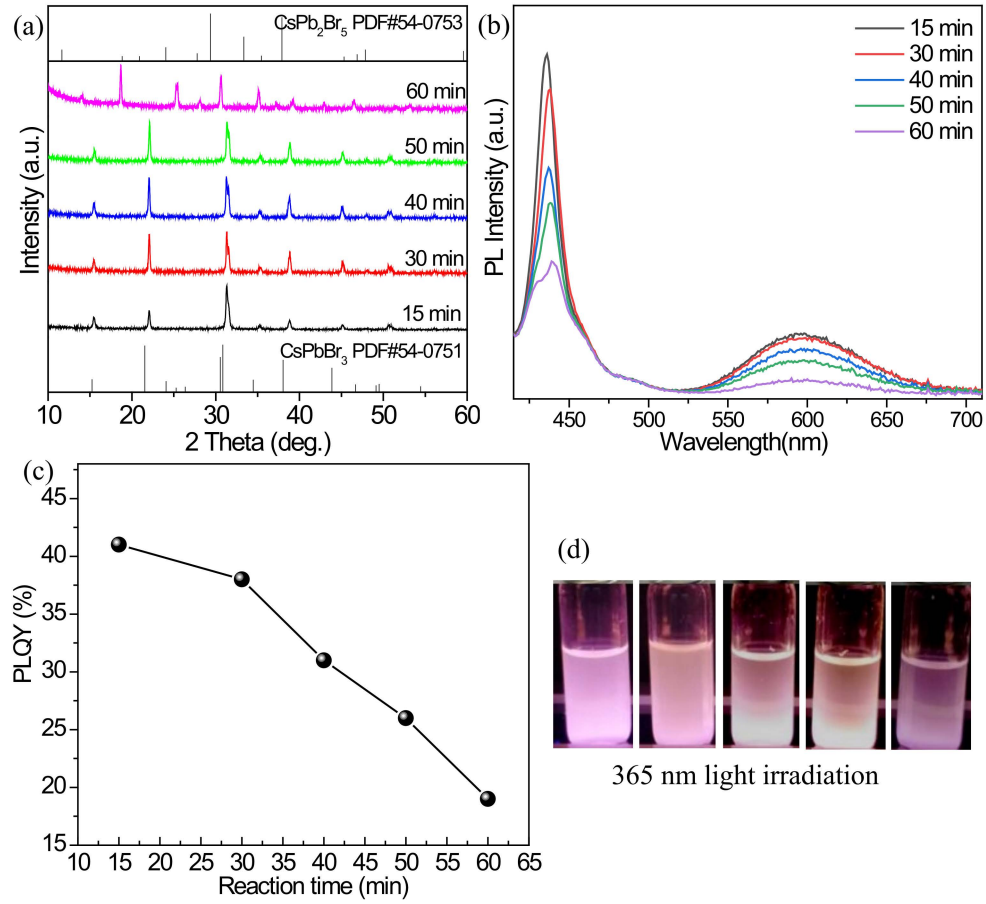

Figure 3. (**a**) XRD patterns, (**b**) PL emission spectra, and (**c**) PLQYs of the Mn^{2+}-doped products fabricated with different reaction times. (**d**) Optical images of the cyclohexane solutions containing the Mn^{2+}-doped products under the environment of 365 nm light: from left to right, the reaction times are 15, 30, 40, 50, and 60 min, respectively.

3.2.4. Effect of Mn^{2+} Source

Different Mn^{2+} sources have different effects on the doping of Mn^{2+} and the overall luminescence of the perovskites due to the presence of different anions. Under the Mn^{2+}/Pb^{2+} feeding ratio of 2/1, temperature of 200 °C, ODE/DGBE volume ratio of 1/1, and reaction time of 30 min, the products obtained by using $C_{10}H_{14}MnO_4$, $C_4H_6MnO_4{\cdot}4H_2O$ and $MnBr_2{\cdot}4H_2O$ as Mn sources have high crystallinity, and their diffraction peaks correspond to the standard card PDF#54-0751 of $CsPbBr_3$ (Figure 5a), whose redshift is not obvious. As for the Mn sources of $MnSO_4{\cdot}H_2O$ and $MnCl_2{\cdot}4H_2O$, the obtained diffraction peaks are remarkably weakened, and the redshift is present, especially for the product synthesized with $MnCl_2{\cdot}4H_2O$. Figure 5b shows the fluorescence spectra of the products synthesized with different Mn sources. Under the excitation of 365 nm UV light, only the product derived from $MnCl_2{\cdot}4H_2O$ exhibits strong exciton and Mn^{2+} emissions, and the highest PLQY of 98% is achieved (Figure 5c). In the case of $C_4H_6MnO_4{\cdot}4H_2O$ and $C_{10}H_{14}MnO_4$, the products obtained have almost no fluorescence. With the doping sources of $MnBr_2{\cdot}4H_2O$ and $MnSO_4{\cdot}H_2O$, the products only have exciton emissions, and their characteristic peaks of Mn^{2+} are very weak (Figure S8). Under the excitation of 365 nm UV light, the products

with different Mn sources show different luminescence colors (Figure 5d), corresponding to their respective fluorescence spectra. Therefore, $MnCl_2$ is the most suitable Mn source for Mn^{2+} post-doping under microwave reaction condition, while $MnBr_2$ with halogen element Br cannot be successfully doped Mn^{2+} into $CsPbBr_3$, indicating the ion exchange of Br^- and Cl^- is important for the doping of Mn^{2+} ions, which is consistent with the previous results [12,36]. One possible reason reported by Liu et al. is that the similar bond energy favors the doping of Mn^{2+} into $CsPbCl_3$ [12]. It is noted that, with the introduction of $MnCl_2{\cdot}4H_2O$, the ion exchange between Br^- and Cl^- is first occurred, resulting in the formation of Pb−Cl bond with a dissociation energy of 301 kJ/mol, which is close to that (338 kJ/mol) of Mn−Cl bond, so the doping of Mn^{2+} in $CsPb(Cl/Br)_3$ can then be realized. As the Mn−Br bond in $MnBr_2$, its dissociation energy (314 kJ/mol) is much stronger than that (249 kJ/mol) of Pb−Br bond, and the Mn^{2+} doped effect can be inhibited due to the extended domains of MnX_2 over a dispersion of Mn^{2+} within the perovskite lattice [12].

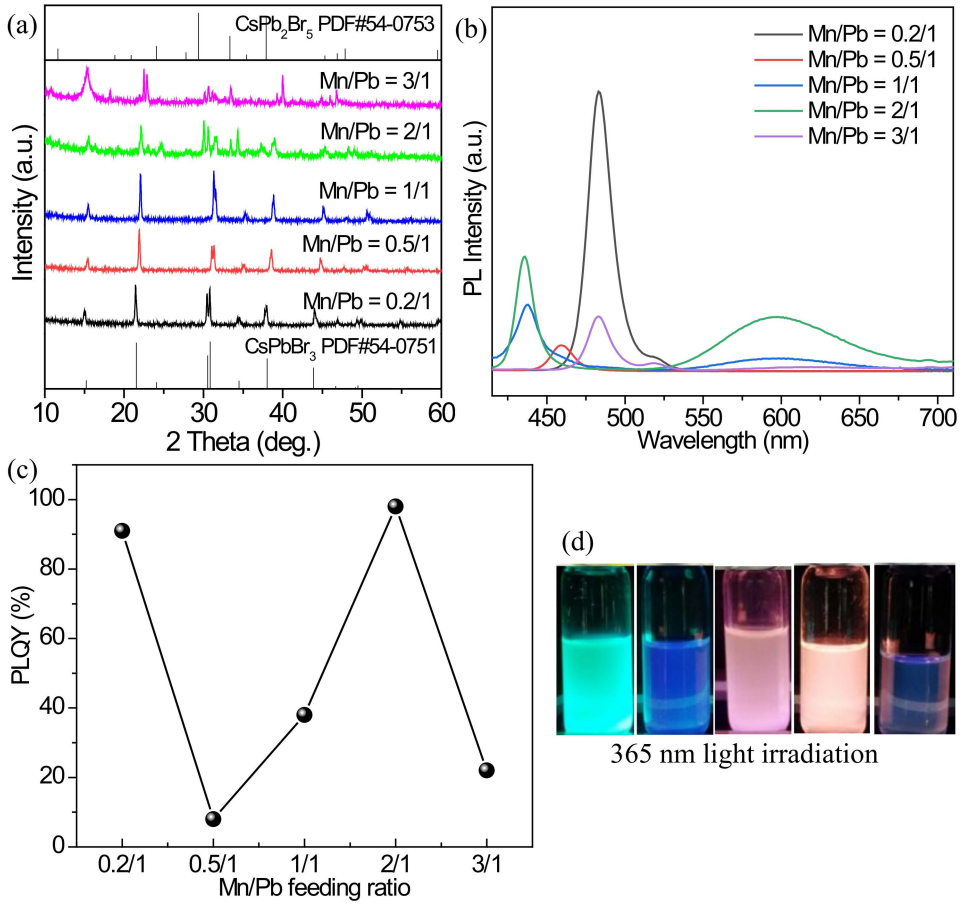

Figure 4. (**a**) XRD patterns, (**b**) PL emission spectra, and (**c**) PLQYs of the Mn^{2+}-doped products fabricated with different Mn^{2+}/Pb^{2+} feeding ratios. (**d**) Optical images of the cyclohexane solutions containing the Mn^{2+}-doped products under the environments of natural and 365 nm light: from left to right, the Mn^{2+}/Pb^{2+} feeding ratios are 0.2/1, 0.5/1, 1/1, 2/1, and 3/1, respectively.

3.2.5. Effect of ODE/DGBE Ratio

DGBE is a polar solvent that acts as a messenger of energy in the microwave reaction process. It absorbs the energy generated by microwave and then heats the solution to help the reaction be completed successfully, so the amount of DGBE also plays a very important role in the postsynthesis of the Mn^{2+} doped inorganic perovskites. The effect of the volume ratio of ODE/DGBE on the products is investigated under the conditions of $MnCl_2{\cdot}4H_2O$ source, Mn^{2+}/Pb^{2+} feeding ratio of 2/1, temperature of 200 °C, and reaction time of 30 min. When the ODE/DGBE ratios are changed from 5/2.5 to 5/5, the redshifted

diffraction peaks of the products are present compared with the standard card PDF#54-0751 of $CsPbBr_3$ (Figure 6a). At the ODE/DGBE ratios of 5/7.5 and 5/10, some diffraction peaks attributing to $CsPb_2Br_5$ also appear in the products. As the ODE/DGBE ratio further increases to 5/12.5, the intensity of the diffraction peaks largely decreases, indicating the low crystallinity of perovskite phases. The PL emission spectra of the products synthesized with different ODE/DGBE volume ratios are given in Figure 6b. At the low ODE/DGBE ratio of 5/2.5, both the exciton and Mn^{2+} characteristic peaks are weak. When the high ODE/DGBE ratios of 5/10 and 5/12.5 are applied, there are no obvious characteristic emission peaks of Mn^{2+}. The strong Mn^{2+} characteristic peaks are present in the products synthesized with the ODE/DGBE ratios of 5/5 and 5/7.5, and although there is a slight decrease in the intensity of the former, its PLQY (98%) is stronger than that (89%) of the latter (Figure 6c). Therefore, the ODE/DGBE ratio of 5/5 is the most appropriate value for the postsynthesis of the Mn^{2+}-doped product, which emits bright orange light under the excitation of 365 nm UV light (Figure 6d).

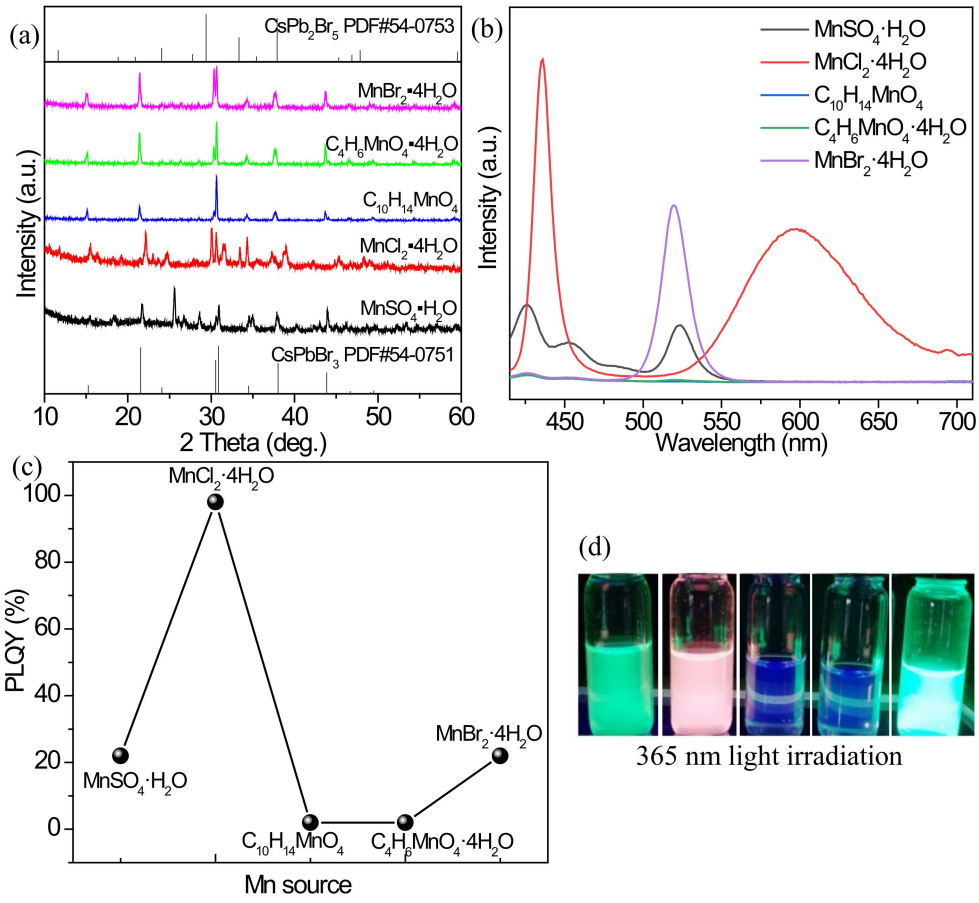

Figure 5. (**a**) XRD patterns, (**b**) PL emission spectra, and (**c**) PLQYs of the Mn^{2+}-doped products fabricated with different Mn^{2+} precursors. (**d**) Optical images of the cyclohexane solutions containing the Mn^{2+}-doped products under the environment of 365 nm light: from left to right, the Mn^{2+} precursors are $MnSO_4{\cdot}H_2O$, $MnCl_2{\cdot}4H_2O$, $C_{10}H_{14}MnO_4$, $C_4H_6MnO_4{\cdot}4H_2O$, and $MnBr_2{\cdot}4H_2O$, respectively.

3.3. Optical Properties before and after Mn^{2+} Doping

According to the above results, the optimum Mn^{2+}-doped product is synthesized by using the $MnCl_2{\cdot}4H_2O$ source and the conditions of a temperature of 200 °C, reaction time of 30 min, Mn^{2+}/Pb^{2+} feeding ratio of 2/1, and ODE/DGBE volume ratio of 5/5, which is marked as $CsPb(Cl/Br)_3$:Mn (Figure S9). As shown in Figure 7a, through Mn^{2+} doping, the exciton fluorescence emission peak of the $CsPbBr_3$ precursor blueshifts from 523 to 437 nm of $CsPb(Cl/Br)_3$:Mn, and although the exciton peak decreases, a large Mn^{2+} characteristic

emission peak at 597 nm is obtained, suggesting the Mn^{2+} ions have been doped into the $CsPbBr_3$ crystals. The Mn^{2+} doping effect can also be demonstrated by the EPR spectrum in Figure 7b, where the single peak with a g value of 2.001 means the Mn^{2+} ions are indeed present in the crystals [37–39], and the lack of six hyperfine splitting profile is caused by the strong exchange interaction between Mn-pairs introduced from the high feeding dosage of Mn^{2+}/Pb^{2+}. The UV-vis absorption spectra of the products before and after Mn^{2+} doping are given in Figure S10, and the initial first excitonic absorption peak at 515 nm is blueshifted to about 436 nm. The PL decay curves of the exciton peaks are given in Figure 7c, and the average PL lifetime (2.46 ns) of $CsPb(Cl/Br)_3$:Mn is much lower than that (49.40 ns) of the $CsPbBr_3$ precursor, indicating there is an efficient energy transfer process from exciton to Mn^{2+}, leading to the generation of the Mn^{2+} emission peak with an average PL lifetime of 0.94 ms (Figure 7d), which is originated from the $^4T_1 \rightarrow {}^6A_1$ transitions of the Mn^{2+} ions [12,32]. The PLQY of the $CsPbBr_3$ precursor is calculated to be 93%, and after Mn^{2+} doping, the total PLQY of the optimum $CsPb(Cl/Br)_3$:Mn improves to 98%. Therefore, Mn^{2+} doping provides the enhanced PL property for the inorganic perovskites.

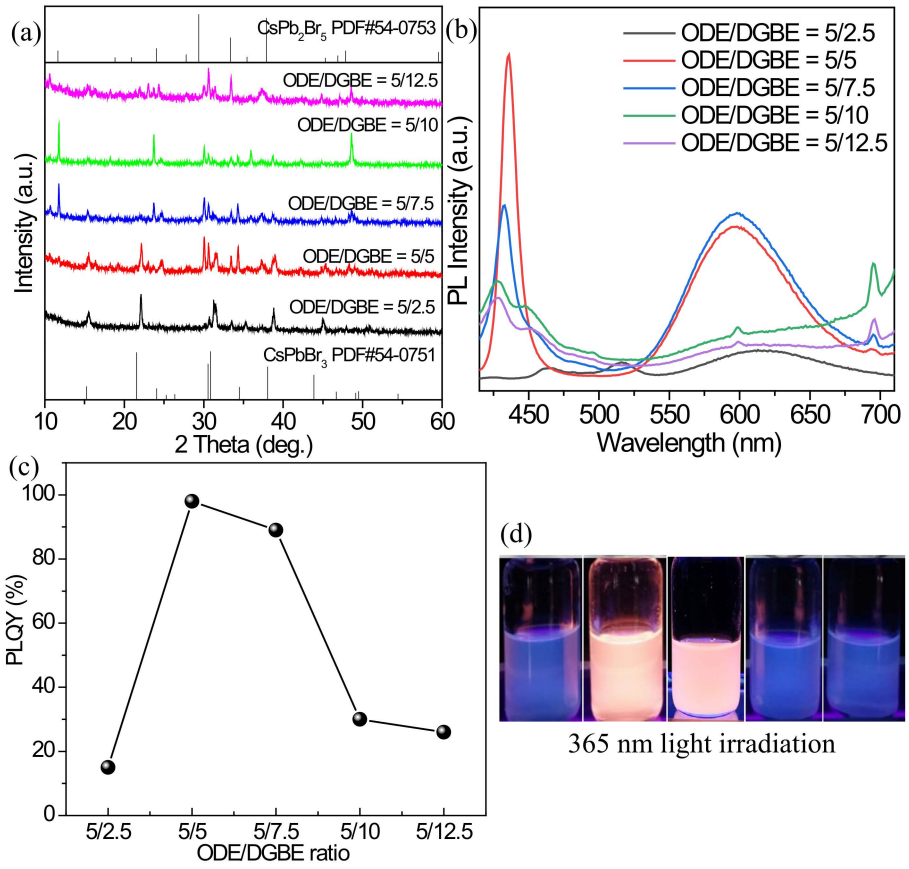

Figure 6. (**a**) XRD patterns, (**b**) PL emission spectra, and (**c**) PLQYs of the Mn^{2+}-doped products fabricated with different ODE/DGBE ratios. (**d**) Optical images of the cyclohexane solutions containing the Mn^{2+}-doped products under the environment of 365 nm light: from left to right, the ODE/DGBE ratios are 5/2.5, 5/5, 5/7.5, 5/10, and 5/12.5, respectively.

3.4. Morphology Evolution before and after Mn^{2+} Doping

The morphology of the $CsPbBr_3$ precursor is analyzed by SEM. As shown in Figure 8a, there are mainly two kinds of particles: small particle aggregates and microcubic particles with an average size of about 3.4 ± 0.4 μm. To distinguish them, the EDS spectra of points 1, 2, 3, and 4 selected from Figure 8a are tested, and the Cs:Pb:Br molar ratios of the small particle aggregates are close to 1:1:3 (Table S1), while those of the microcubic particles are close to 1:2:5. The EDS mapping results of Figure 8a are provided in Figures 8b and S11,

and the Cs signals (red color) in the small particle aggregates are distributed more densely compared with those in the large square particles. According to the crystal phases contained in the $CsPbBr_3$ precursor, it can be indicated that the microcubic particles are attributed to $CsPb_2Br_5$, and the small particle aggregates mainly consist of $CsPbBr_3$ NCs. Figure 8c shows the TEM image of the $CsPbBr_3$ precursor, and the microcubic aggregate particles and cubic NCs can be observed. The corresponding high-resolution TEM (HRTEM) image is given in Figure 8d, and the (020) planes of $CsPbBr_3$ in the cubic NC and the (110) planes of $CsPb_2Br_5$ in the microcubic particle are present in the fast Fourier transform (FFT) patterns (insets of Figure 8d). In combination with the SEM results, it can be inferred that the surface of the $CsPb_2Br_5$ microcubic particles is deposited with many well-separated $CsPbBr_3$ NCs, which ensure the high luminous performance of the $CsPbBr_3$ precursor.

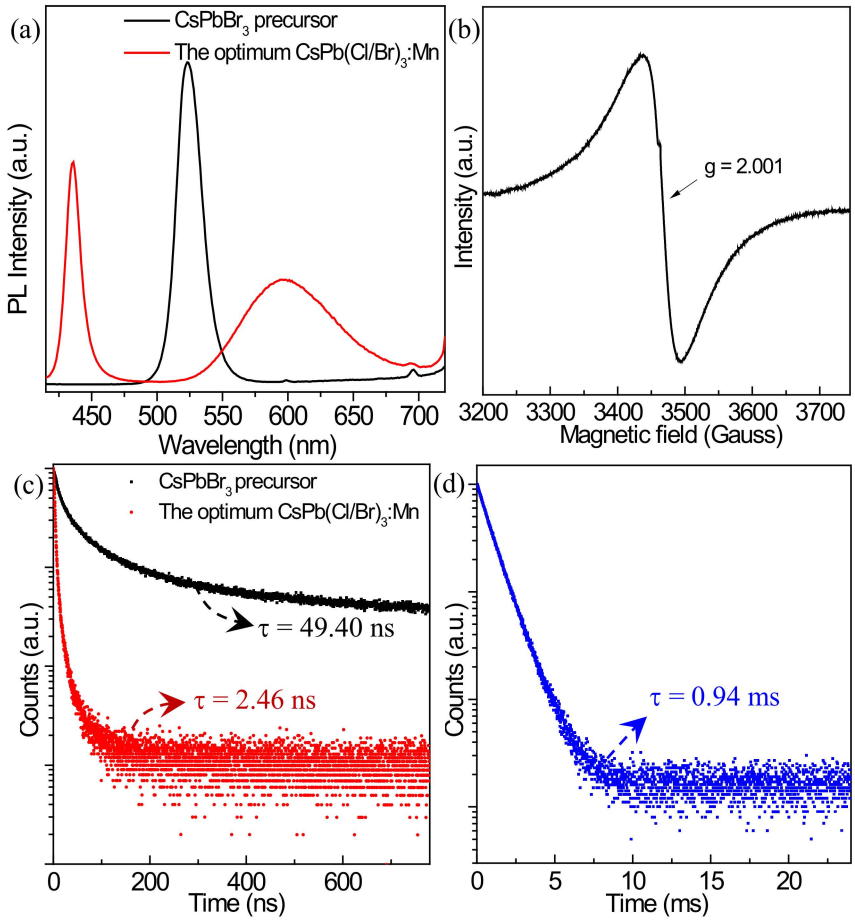

Figure 7. (**a**) PL emission spectra of the $CsPbBr_3$ precursor and the optimum $CsPb(Cl/Br)_3$:Mn product. (**b**) EPR spectrum of the optimum $CsPb(Cl/Br)_3$:Mn product. (**c**) PL decay curves of the $CsPbBr_3$ precursor and $CsPb(Cl/Br)_3$:Mn detected at 523 and 437 nm, respectively, with 370 nm excitation. (**d**) PL decay curve of $CsPb(Cl/Br)_3$:Mn detected at 597 nm with 370 nm excitation.

The SEM morphology of the optimum $CsPb(Cl/Br)_3$:Mn product is shown in Figure 9a, where the aggregate particles consisting of nanoparticles are present. From the TEM image of $CsPb(Cl/Br)_3$:Mn (Figure S12), it can be found that the microcubic particles with an average size of about 3.2 ± 0.3 μm are also present, but they are not attributed to $CsPb_2Br_5$, because it is disappeared after Mn^{2+} doping. Importantly, there are many cubic NCs on the outmost surface of microcubic particles (Figure 9b). To confirm the structure of these NCs, their HRTEM image is tested and shown in Figure 9c. The lattice fringe spacing of the cubic NC is measured to be 0.56 nm, which consists of the (001) planes (FFT pattern of Figure 9c) of the partial Cl^--substituted $CsPb(Cl/Br)_3$:Mn. The high-angle annular dark field scanning TEM (HAADF-STEM) image of $CsPb(Cl/Br)_3$:Mn is provided in Figure S13, and the STEM-

EDS maps of Cs (Figure 9d), Pb (Figure 9e), Mn (Figure 9f), Cl (Figure 9g), and Br (Figure 9h) indicate that they are uniformly distributed throughout the microcubic particle (Figure 9i), including the outmost surface NCs. Therefore, the microcubic particles and their surface NCs are all ascribed to the $CsPb(Cl/Br)_3$:Mn phase, wherein the microcubic morphology is probably inherited from the large $CsPb_2Br_5$ particles, while the presence of the surface well-separated $CsPb(Cl/Br)_3$:Mn NCs is the guarantee of the high PLQY and excellent color-tunable luminescence property of the Mn^{2+} doped product since the contribution from their microcrystals is very limited. The detected molar ratio of Cs:Pb:Br:Cl:Mn is 1:0.99:1.65:3.8:1.3 (Table S1), meaning a certain amount of Mn^{2+} has been doped into the $CsPbBr_3$ precursor to form $CsPb(Cl/Br)_3$:Mn NCs, which possess the obvious Mn^{2+}-related luminescence.

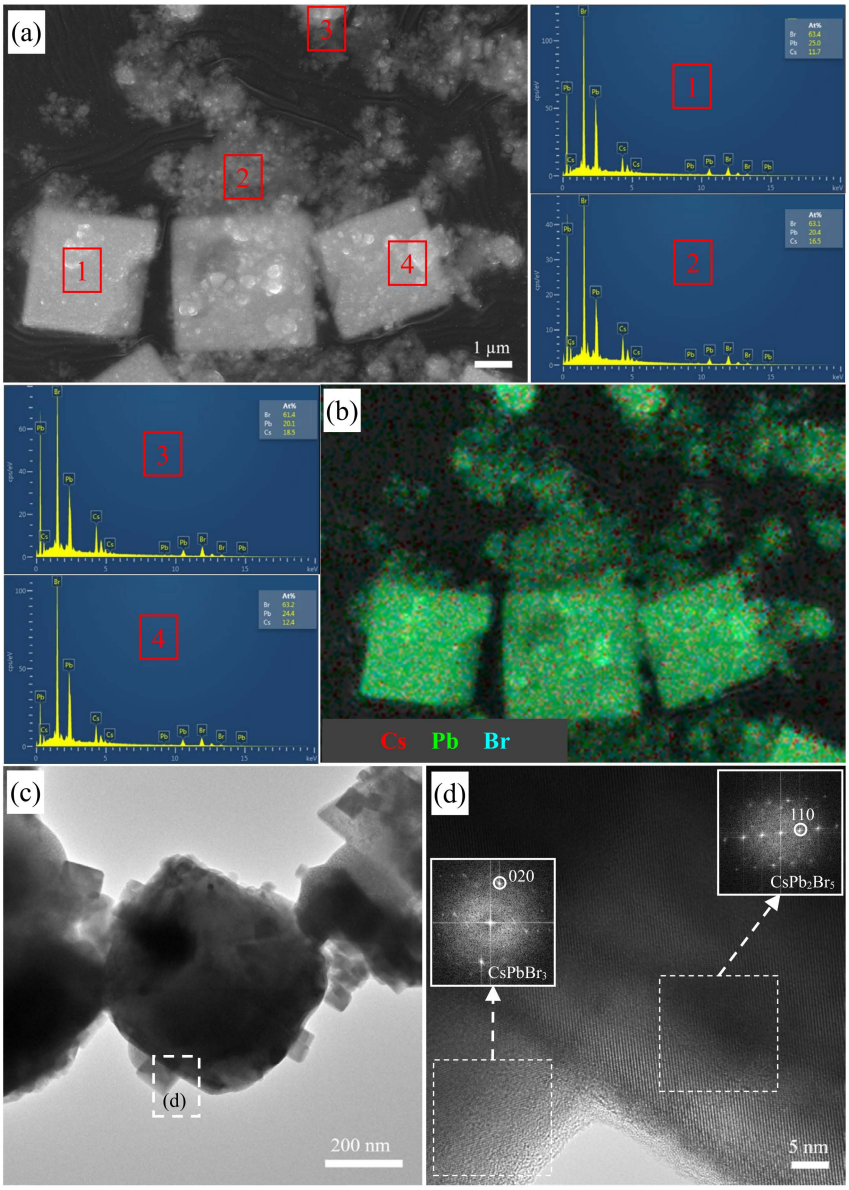

Figure 8. (**a**) SEM image of the $CsPbBr_3$ precursor and its corresponding EDS spectra of the points 1, 2, 3, and 4. (**b**) The elemental overlay of Cs, Pb, and Br for the $CsPbBr_3$ precursor. (**c**) TEM and (**d**) HRTEM images of the $CsPbBr_3$ precursor; insets: FFT patterns.

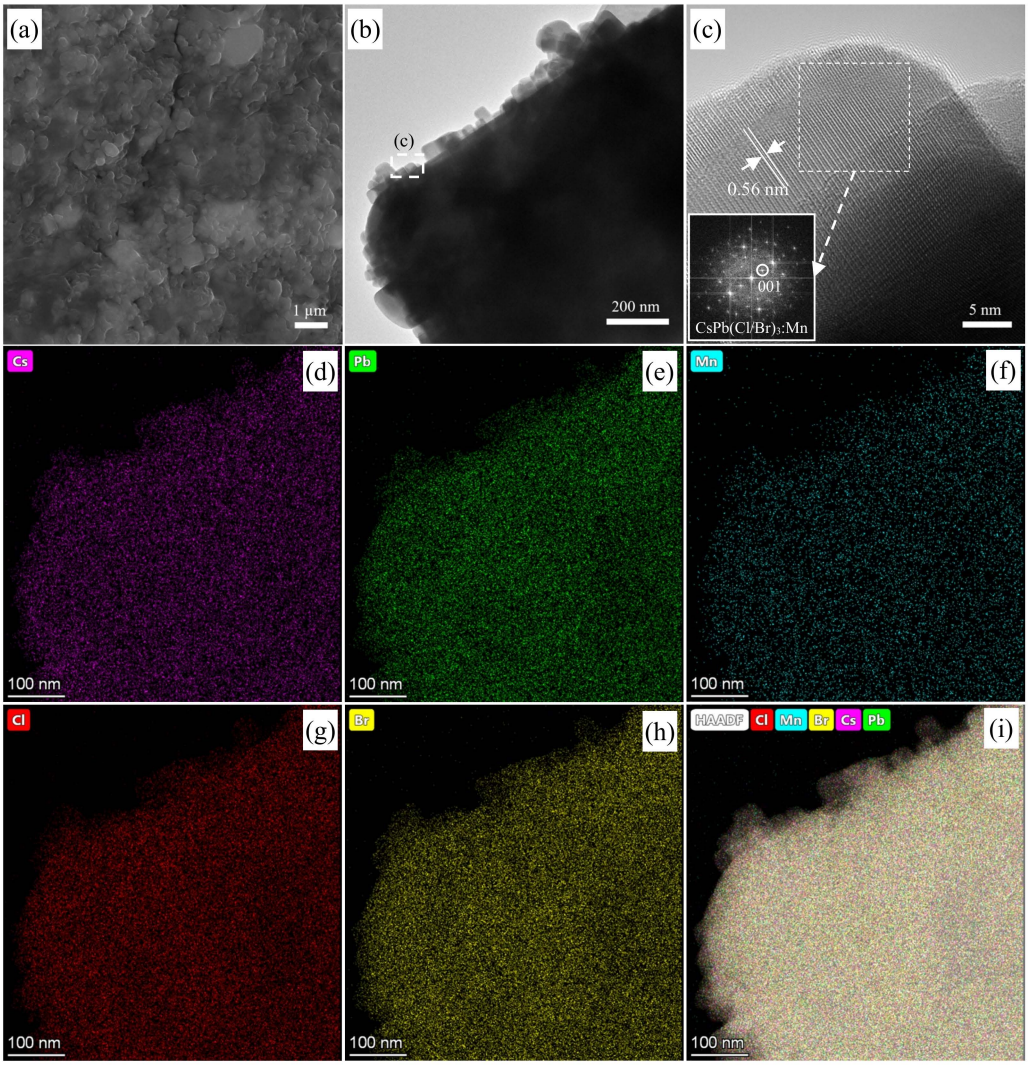

Figure 9. (**a**) SEM, (**b**) TEM and (**c**) HRTEM images of the optimum $CsPb(Cl/Br)_3$:Mn product; inset: FFT pattern. The elemental maps of (**d**) Cs, (**e**) Pb, (**f**) Mn, (**g**) Cl, (**h**) Br, and (**i**) their overlay with the HAADF-STEM image of the optimum $CsPb(Cl/Br)_3$:Mn product.

3.5. XPS Analysis before and after Mn^{2+} Doping

The change of surface composition and chemical states before and after Mn^{2+} doping is investigated by XPS. As shown in the survey scan XPS spectrum of the $CsPbBr_3$ precursor (Figure 10a), the elements Cs, Pb, Br, C, O, and Si are detected, where the C and O signals are mainly generated from the residual surface ligands, such as OA, OLA, ODE, and DGBE, and the Si signal is produced by the used glass substrate. After Mn^{2+} doping treatment with $MnCl_2{\cdot}4H_2O$, the additional spectroscopic signatures of Mn and Cl appear in the optimum $CsPb(Cl/Br)_3$:Mn product. The high-resolution Cs 3d spectra are shown in Figure 10b, where two peaks corresponding to Cs $3d_{3/2}$ and Cd $3d_{5/2}$ are recorded. The binding energies of the $CsPbBr_3$ precursor are at 738.2 and 724.3 eV, which respectively shift to higher values of 738.3 and 724.4 eV for $CsPb(Cl/Br)_3$:Mn. For the Pb 4f spectra (Figure 10c), two obvious peaks at 143.2 and 138.3 eV for the $CsPbBr_3$ precursor and those at 143.5 and 138.6 eV for $CsPb(Cl/Br)_3$:Mn are detected. The Br 3d spectra can be resolved into two peaks at 69.4 and 68.3 eV for the $CsPbBr_3$ precursor and those at 69.5 and 68.5 eV for $CsPb(Cl/Br)_3$:Mn (Figure 10d). As a result, after Mn^{2+} doping, the Pb 4f and Br 3d peaks also shift to higher binding energies, which should be caused by the modified chemical environment and changed electron density [36]. The Cl 2p spectrum of $CsPb(Cl/Br)_3$:Mn is given in Figure 10e, and the two peaks at 199.8 and 198.2 eV are ascribed to Cl $2p_{1/2}$ and Cl

$2p_{3/2}$, respectively. Figure 10f shows the Mn 2p spectrum of $CsPb(Cl/Br)_3$:Mn, and three peaks can be fit. The peaks at 653.5 and 641.5 eV are attributed to Mn $2p_{1/2}$ and Mn $2p_{3/2}$, respectively, and the peak at 645.7 eV is assigned to the Mn 2p core level [36], meaning Mn^{2+} ions have been successfully doped into the crystal lattice of $CsPbBr_3$. According to the XPS results, the molar ratio of Cs:Pb:Br for the $CsPbBr_3$ precursor is calculated to be 1:1.7:13.2 (Table S1), indicating its surface is enriched with Br element. After Mn^{2+} doping, the Cs:Pb:Br:Cl:Mn molar ratio is calculated to be 1:2.5:8.2:7.1:1.4 for $CsPb(Cl/Br)_3$:Mn, and its surface is also enriched with the halogen elements. These excess halogen signals are different from the results obtained from SEM-EDS and STEM-EDS (Table S1), which may be caused by the excess introduced $PbBr_2$, $MnCl_2$, and organic capping ligands in the synthesis process. However, the XPS results have proved that there are a certain number of Mn^{2+} and Cl^- ions located on the outmost surface of $CsPb(Cl/Br)_3$:Mn NCs.

3.6. Stability before and after Mn^{2+} Doping

The thermal stabilities of the perovskite materials before and after Mn^{2+} doping are first investigated by the temperature-dependent PL experiments. The PL spectra of the $CsPbBr_3$ precursor at temperatures varying from 25 to 135 °C are shown in Figure 11a. It can be found that, with the increase in temperature, the PL peak at 523 nm decreases significantly. When the temperature reaches 135 °C, almost no PL emission is found for the $CsPbBr_3$ precursor. Figure 11b shows the PL spectra of the optimum $CsPb(Cl/Br)_3$:Mn product tested at the temperatures change from 25 to 185 °C. With the increase in temperature, the exciton emission peak at 437 nm and the Mn^{2+} emission peak at 597 nm decreases synchronously. At 135 °C, two distinct emission peaks could still be seen, and the remnant PL of the exciton emission peak is about 5.04%, which is higher than that (0.93%) of the $CsPbBr_3$ precursor (Figure S14a). The corresponding PL positions of the exciton emissions are provided in Figure S14b, and the change range (437 to 439.5 nm) of $CsPb(Cl/Br)_3$:Mn is smaller than that (523 to 527 nm) of the $CsPbBr_3$ precursor. All these indicate that $CsPb(Cl/Br)_3$:Mn has higher thermal stability compared with that of the $CsPbBr_3$ precursor.

To further compare the stability of the products before and after Mn^{2+} doping, their PL emission spectra after storing in air for one year are tested. As shown in Figure 11c, the PL decrease in the $CsPbBr_3$ precursor and $CsPb(Cl/Br)_3$:Mn is not obvious, and high PLQYs of 86% and 93% are respectively maintained after one year. Figure 11d–g shows the optical images of them, and the luminescence color of the $CsPbBr_3$ precursor is changed from bright green (Figure 11d) to bright orange (Figure 11f) for $CsPb(Cl/Br)_3$:Mn, which almost maintain the same even after one year. The maintenance of the PLQYs and the color-tunable luminescence properties suggests the high stability of the products fabricated by using microwave heating.

On the basis of the above morphology and composition analysis (Figures 8 and 10), there are two crystal phases of $CsPbBr_3$ and $CsPb_2Br_5$ contained in the $CsPbBr_3$ precursor, where the $CsPbBr_3$ NCs are dispersed on the surface of the $CsPb_2Br_5$ microcubic crystals with sizes of about 3.4 ± 0.4 μm. These well-separated $CsPbBr_3$ NCs are responsible for the strong 523 nm PL emission of the precursor (Figures 7 and 12), while the $CsPb_2Br_5$ microcubic crystals can be taken as the substrates to embed $CsPbBr_3$ NCs to boost their stability. After the post-doping of Mn^{2+} ions, the $CsPb_2Br_5$ phase disappeared, and the redshifted diffraction peaks of $CsPb(Cl/Br)_3$:Mn appeared (Figures 4a–6a. In terms of the morphology and composition of $CsPb(Cl/Br)_3$:Mn (Figures 9,10 and S12), there are also microcubic crystals with sizes of about 3.2 ± 0.3 μm and NCs. These microcubic crystals are very likely formed from the $CsPb_2Br_5$ phases after their ion exchange of Br^- by Cl^- and the doping of Mn^{2+} ions. Meanwhile, the $CsPb(Cl/Br)_3$:Mn NCs can also be produced from the $CsPbBr_3$ NCs and maintain their positions to be uniformly and tightly dispersed on the surface of the $CsPb(Cl/Br)_3$:Mn microcubic crystals (Figure 12). Furthermore, the surface organic capping ligands of the $CsPbBr_3$, $CsPb_2Br_5$, and $CsPb(Cl/Br)_3$:Mn are almost the same (Figure S15) [40,41]. Therefore, the physical and chemical adsorptions may be present

for the interaction between the NCs and the microcubic crystals, which greatly enhance the stability of the system. It is worth noting that although the microsized perovskite crystals are formed from this microwave-assisted method, the NCs can be generated and embedded on the surface of the microcubic crystals, leading to the formation of excellent color-tunable luminescent perovskite materials with high stability.

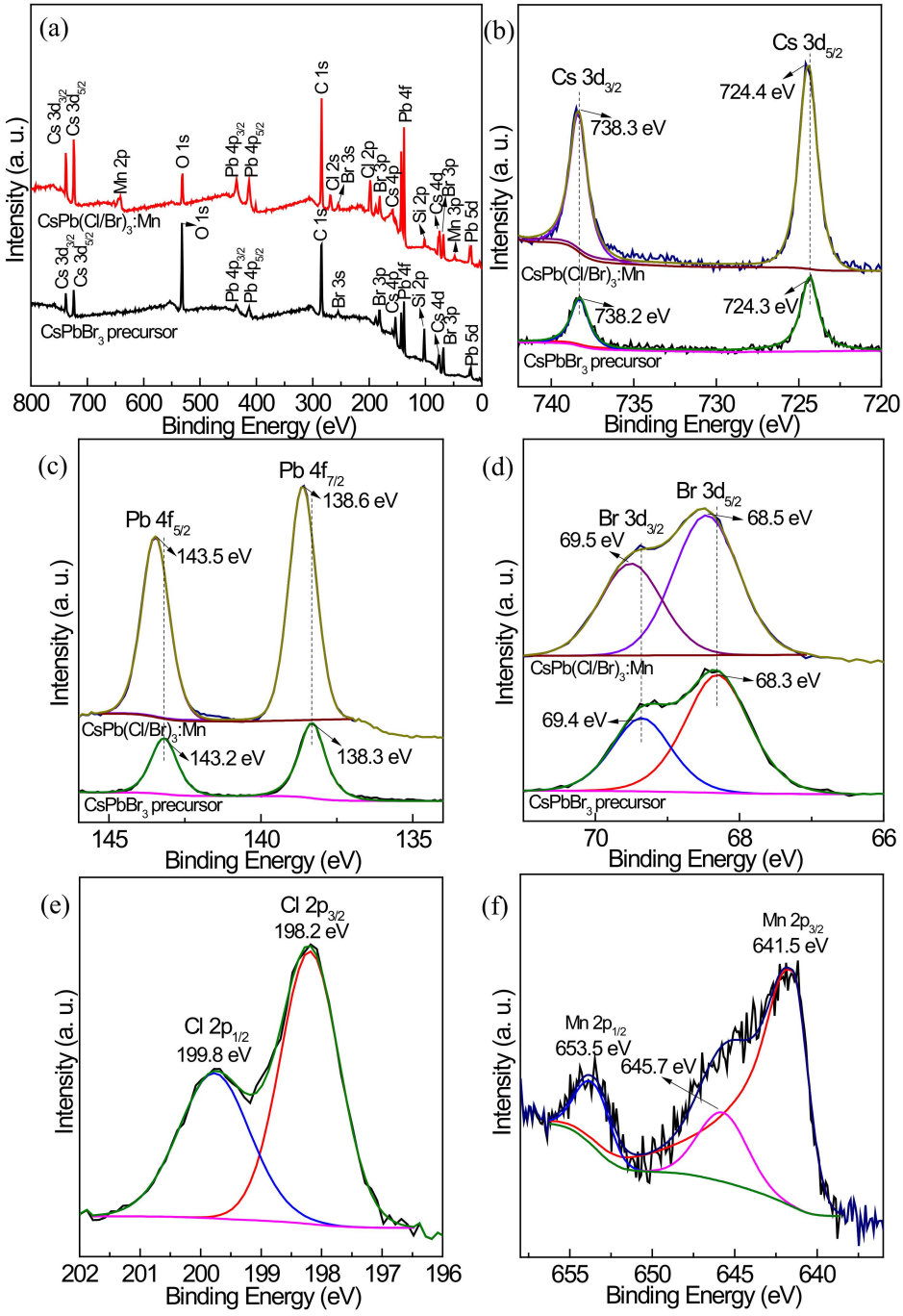

Figure 10. (**a**) Survey scan XPS spectra of the $CsPbBr_3$ precursor and the optimum $CsPb(Cl/Br)_3$:Mn product and their high-resolution XPS spectra of (**b**) Cs 3d, (**c**) Pb 4f, and (**d**) Br 3d. High-resolution XPS spectra of the optimum $CsPb(Cl/Br)_3$:Mn product: (**e**) Cl 2p and (**f**) Mn 2p.

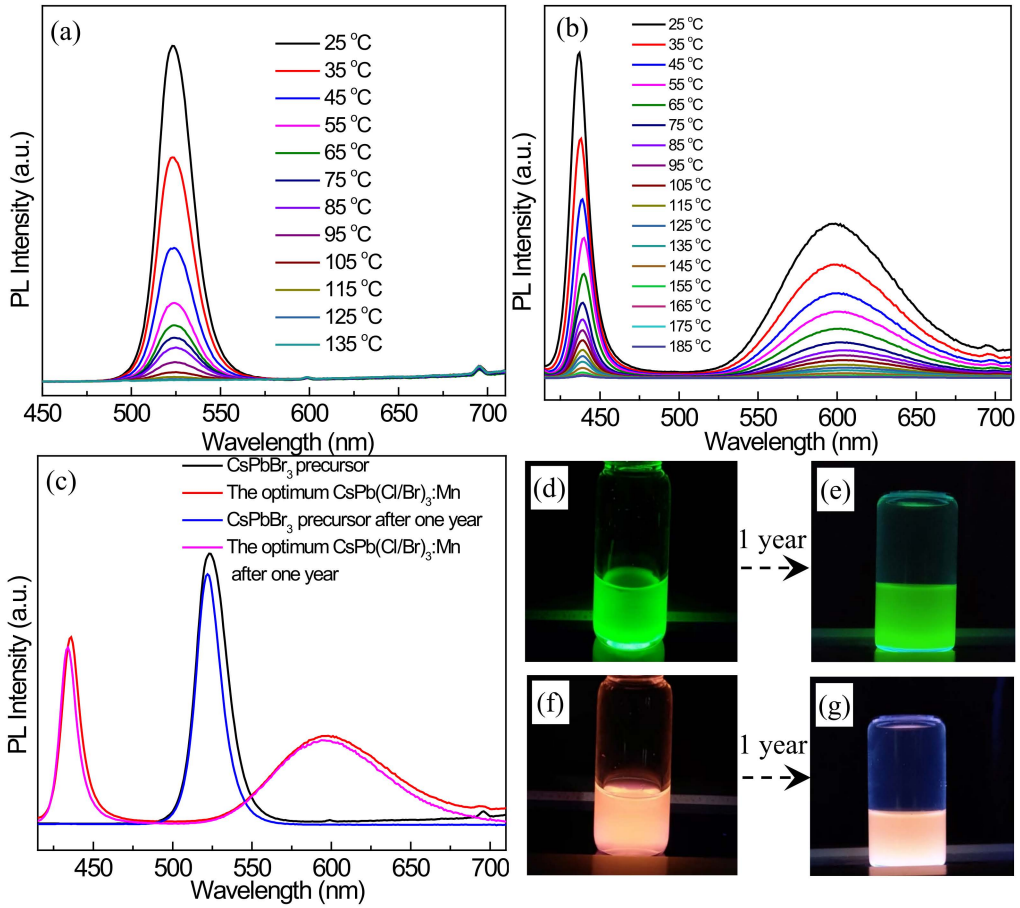

Figure 11. PL emission spectra of (**a**) the $CsPbBr_3$ precursor and (**b**) the optimum $CsPb(Cl/Br)_3$:Mn product as the treatment temperatures increase. (**c**) PL emission spectra of the $CsPbBr_3$ precursor and the optimum $CsPb(Cl/Br)_3$:Mn product before and after storing in air for one year. Optical images of the cyclohexane solutions containing (**d**,**e**) the $CsPbBr_3$ precursor and (**f**,**g**) the optimum $CsPb(Cl/Br)_3$:Mn product under the environment of 365 nm light before and after storing in air for one year.

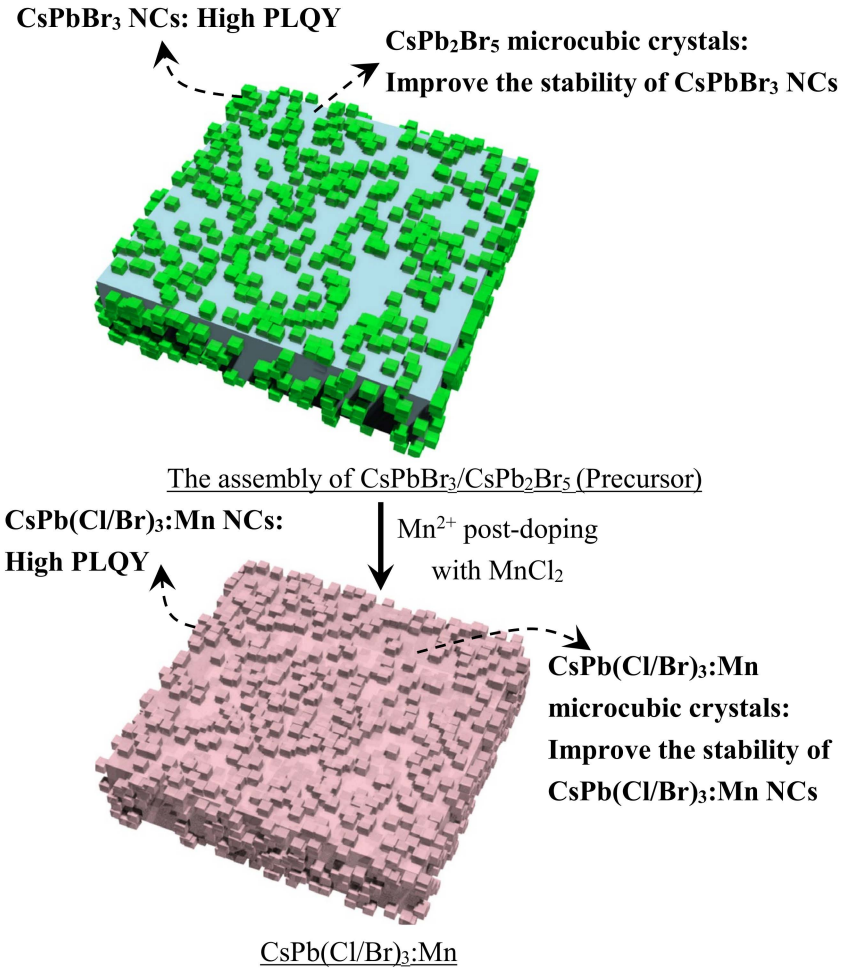

Figure 12. Schematics of PL and stability enhancement mechanism of the $CsPbBr_3$ precursor and the optimum $CsPb(Cl/Br)_3$:Mn product.

4. Conclusions

The assembly of $CsPbBr_3$ NCs deposited on $CsPb_2Br_5$ microcubic crystals is initially prepared by a microwave method, where the feed mole ratio of $CsCO_3/PbBr_2$, temperature, and volume ratio of ODE/DGBE are investigated, and the sample with best luminescent performance is used as the precursor. The Mn^{2+} post-doping experiments are based on the precursor. The effects of reaction temperatures, times, Mn^{2+}/Pb^{2+} feeding ratios, Mn^{2+} sources, and ODE/DGBE ratios are performed, and the optimum $CsPb(Cl/Br)_3$:Mn product is achieved. With the introduction of $MnCl_2{\cdot}4H_2O$, the exciton fluorescence emission peak of the $CsPbBr_3$ precursor is blueshifted from 523 to 437 nm of $CsPb(Cl/Br)_3$:Mn due to the partial substitution of Br^- by Cl^-, and a new Mn^{2+} characteristic emission peak at 597 nm is produced. For the $CsPbBr_3$ precursor, the high PLQY is generated from the well-separated $CsPbBr_3$ NCs on the $CsPb_2Br_5$ microcubic crystals, which also improve the stability of $CsPbBr_3$ NCs. After Mn^{2+}-doping treatment, the microcubic crystal shape of $CsPb_2Br_5$ shape is kept to form $CsPb(Cl/Br)_3$:Mn microcrystals, whose surface is also well dispersed and embedded with $CsPb(Cl/Br)_3$:Mn NCs to gain high PLQY and stability.

Supplementary Materials: The following supporting information can be downloaded at: https://www.mdpi.com/article/10.3390/nano12152535/s1. Figures S1–S4, S7, S8, and S9: PL emission spectra, Figures S5 and S6: XRD patterns, Figure S10: UV-vis absorption spectra, Table S1: Element contents, Figure S11: Elemental maps, Figure S12: TEM image, Figure S13: HAADF-STEM image, and Figure S14: The changes of PL peak intensities and positions of the products. References [40,41] are cited in the supplementary materials.

Author Contributions: Conceptualization, Y.Z. and S.H.; Data curation, Y.Z., J.T. and G.H.; Formal analysis, Y.Z., C.F. and S.H.; Funding acquisition, Y.Z. and S.H.; Investigation, X.Q., W.Z. and J.W.; Methodology, C.F. and S.H.; Project administration, Y.Z. and S.H.; Supervision, S.H.; Writing—original draft, Y.Z. and Y.F.; Writing—review and editing, S.H. All authors have read and agreed to the published version of the manuscript.

Funding: This research was funded by the National Natural Science Foundation of China (51872129), the Natural Science Foundation of Jiangsu Province (BK20201471, BK20211360, and BK20191038), the Natural Science Foundation of the Jiangsu Higher Education Institutions of China (19KJA460001), Industry-University-Research Cooperation Project of Jiangsu Province (BY2021339), and the Talent Introduction Project of Jiangsu University of Technology (KYY17002).

Institutional Review Board Statement: Not applicable.

Informed Consent Statement: Not applicable.

Data Availability Statement: The data is available on reasonable request from the corresponding author.

Conflicts of Interest: The authors declare no conflict of interest.

References

1. Stranks, S.D.; Snaith, H.J. Metal-halide perovskites for photovoltaic and light-emitting devices. *Nat. Nanotechnol.* **2015**, *10*, 391–402. [CrossRef] [PubMed]
2. Park, N.-G.; Grätzel, M.; Miyasaka, T.; Zhu, K.; Emery, K. Towards stable and commercially available perovskite solar cells. *Nat. Energy* **2016**, *1*, 16152. [CrossRef]
3. Protesescu, L.; Yakunin, S.; Bodnarchuk, M.I.; Krieg, F.; Caputo, R.; Hendon, C.H.; Yang, R.X.; Walsh, A.; Kovalenko, M.V. Nanocrystals of cesium lead halide perovskites ($CsPbX_3$, X = Cl, Br, and I): Novel optoelectronic materials showing bright emission with wide color gamut. *Nano Lett.* **2015**, *15*, 3692–3696. [CrossRef] [PubMed]
4. Nedelcu, G.; Protesescu, L.; Yakunin, S.; Bodnarchuk, M.I.; Grotevent, M.J.; Kovalenko, M.V. Fast anion-exchange in highly luminescent nanocrystals of cesium lead halide perovskites ($CsPbX_3$, X = Cl, Br, I). *Nano Lett.* **2015**, *15*, 5635–5640. [CrossRef] [PubMed]
5. Ma, T.; Wang, S.; Zhang, Y.; Zhang, K.; Yi, L. The development of all-inorganic $CsPbX_3$ perovskite solar cells. *J. Mater. Sci.* **2019**, *55*, 464–479. [CrossRef]
6. He, S.; Han, Y.; Guo, J.; Wu, K. Long-lived delayed emission from $CsPbBr_3$ perovskite nanocrystals for enhanced photochemical reactivity. *ACS Energy Lett.* **2021**, *6*, 2786–2791. [CrossRef]
7. Li, X.; Wu, Y.; Zhang, S.; Cai, B.; Gu, Y.; Song, J.; Zeng, H. $CsPbX_3$ quantum dots for lighting and displays: Room-temperature synthesis, photoluminescence superiorities, underlying origins and white light-emitting diodes. *Adv. Funct. Mater.* **2016**, *26*, 2435–2445. [CrossRef]
8. Yang, Y.; You, J. Make perovskite solar cells stable. *Nature* **2017**, *544*, 155–156. [CrossRef]
9. Huang, S.; Wang, B.; Zhang, Q.; Li, Z.; Shan, A.; Li, L. Postsynthesis potassium-modification method to improve stability of $CsPbBr_3$ perovskite nanocrystals. *Adv. Optical Mater.* **2018**, *6*, 1701106. [CrossRef]
10. He, X.; Qiu, Y.; Yang, S. Fully-inorganic trihalide perovskite nanocrystals: A new research frontier of optoelectronic materials. *Adv. Mater.* **2017**, *29*, 1700775. [CrossRef]
11. Swarnkar, A.; Mir, W.J.; Nag, A. Can B-site doping or alloying improve thermal- and phase-stability of all-inorganic $CsPbX_3$ (X = Cl, Br, I) perovskites? *ACS Energy Lett.* **2018**, *3*, 286–289. [CrossRef]
12. Liu, W.; Lin, Q.; Li, H.; Wu, K.; Robel, I.; Pietryga, J.M.; Klimov, V.I. Mn^{2+}-doped lead halide perovskite nanocrystals with dual-color emission controlled by halide content. *J. Am. Chem. Soc.* **2016**, *138*, 14954–14961. [CrossRef]
13. Yao, Z.; Zhao, W.; Chen, S.; Jin, Z.; Liu, S.F. Mn doping of $CsPbI_3$ film towards high-efficiency solar cell. *ACS Appl. Energy Mater.* **2020**, *3*, 5190–5197. [CrossRef]
14. Liu, W.; Zheng, J.; Cao, S.; Wang, L.; Gao, F.; Chou, K.-C.; Hou, X.; Yang, W. Mass production of Mn^{2+}-doped $CsPbCl_3$ perovskite nanocrystals with high quality and enhanced optical performance. *Inorg. Chem. Front.* **2018**, *5*, 2641–2647. [CrossRef]
15. Dong, L.; Chen, Z.; Ye, L.; Yu, Y.; Zhang, J.; Liu, H.; Zang, J. Gram-scale synthesis of all-inorganic perovskite quantum dots with high Mn substitution ratio and enhanced dual-color emission. *Nano Res.* **2019**, *12*, 1733–1738. [CrossRef]
16. Zhao, Y.; Xie, C.; Zhang, X.; Matras-Postolek, K.; Yang, P. Mn:$CsPbBr_3$ nanoplatelets for bright white-emitting displays. *ACS Appl. Nano Mater.* **2021**, *4*, 6223–6230. [CrossRef]
17. Sun, Y.; Chen, J.; Wang, F.; Yin, Y.; Jin, Y.; Wang, J.; Peng, X.; Han, R.; Zhang, C.; Kong, J.; et al. Direct fabrication of $CsPb_xMn_{1-x}(Br,Cl)_3$ thin film by a facile solution spraying approach. *Nanomaterials* **2021**, *11*, 3242. [CrossRef] [PubMed]
18. Chen, D.; Zhou, S.; Tian, F.; Ke, H.; Jiang, N.; Wang, S.; Peng, Y.; Liu, Y. Halogen-hot-injection synthesis of Mn-doped $CsPb(Cl/Br)_3$ nanocrystals with blue/orange dual-color luminescence and high photoluminescence quantum yield. *Adv. Opt. Mater.* **2019**, *7*, 1901082. [CrossRef]

19. Mir, W.J.; Mahor, Y.; Lohar, A.; Jagadeeswararao, M.; Das, S.; Mahamuni, S.; Nag, A. Postsynthesis doping of Mn and Yb into $CsPbX_3$ (X = Cl, Br, or I) perovskite nanocrystals for downconversion emission. *Chem. Mater.* **2018**, *30*, 8170–8178. [CrossRef]
20. Parobek, D.; Roman, B.J.; Dong, Y.; Jin, H.; Lee, E.; Sheldon, M.; Son, D.H. Exciton-to-dopant energy transfer in Mn-doped cesium lead halide perovskite nanocrystals. *Nano Lett.* **2016**, *16*, 7376–7380. [CrossRef] [PubMed]
21. Zou, S.; Liu, Y.; Li, J.; Liu, C.; Feng, R.; Jiang, F.; Li, Y.; Song, J.; Zeng, H.; Hong, M.; et al. Stabilizing cesium lead halide perovskite lattice through Mn(II) substitution for air-stable light-emitting diodes. *J. Am. Chem. Soc.* **2017**, *139*, 11443–11450. [CrossRef]
22. Cheng, J.; Li, Y.; Qu, W.; Sun, M.; Liu, Y.; Shi, W.; Du, W.; Zhang, Y. Mechanochemical synthesis and characterization of Mn-doped $CsPbCl_3$ perovskite nanocrystals. *J. Alloys Compd.* **2020**, *822*, 1901082. [CrossRef]
23. Begum, R.; Parida, M.R.; Abdelhady, A.L.; Murali, B.; Alyami, N.M.; Ahmed, G.H.; Hedhili, M.N.; Bakr, O.M.; Mohammed, O.F. Engineering Interfacial Charge Transfer in $CsPbBr_3$ Perovskite Nanocrystals by Heterovalent Doping. *J. Am. Chem. Soc.* **2017**, *139*, 731–737. [CrossRef] [PubMed]
24. Liu, H.; Wu, Z.; Shao, J.; Yao, D.; Gao, H.; Liu, Y.; Yu, W.; Zhang, H.; Yang, B. $CsPb_xMn_{1-x}Cl_3$ perovskite quantum dots with high Mn substitution ratio. *ACS Nano* **2017**, *11*, 2239–2247. [CrossRef]
25. Yuan, X.; Ji, S.; De Siena, M.C.; Fei, L.; Zhao, Z.; Wang, Y.; Li, H.; Zhao, J.; Gamelin, D.R. Photoluminescence temperature dependence, dynamics, and quantum efficiencies in Mn^{2+}-doped $CsPbCl_3$ perovskite nanocrystals with varied dopant concentration. *Chem. Mater.* **2017**, *29*, 8003–8011. [CrossRef]
26. Liu, H.; Wu, Z.; Gao, H.; Shao, J.; Zou, H.; Yao, D.; Liu, Y.; Zhang, H.; Yang, B. One-step preparation of cesium lead halide $CsPbX_3$ (X = Cl, Br, and I) perovskite nanocrystals by microwave irradiation. *ACS Appl. Mater. Interfaces* **2017**, *9*, 42919–42927. [CrossRef]
27. Hu, Q.; Li, Z.; Tan, Z.; Song, H.; Ge, C.; Niu, G.; Han, J.; Tang, J. Rare earth ion-doped $CsPbBr_3$ nanocrystals. *Adv. Opt. Mater.* **2018**, *6*, 1700864. [CrossRef]
28. Mir, W.J.; Jagadeeswararao, M.; Das, S.; Nag, A. Colloidal Mn-doped cesium lead halide perovskite nanoplatelets. *ACS Energy Lett.* **2017**, *2*, 537–543. [CrossRef]
29. Zhu, J.; Yang, X.; Zhu, Y.; Wang, Y.; Cai, J.; Shen, J.; Sun, L.; Li, C. Room-temperature synthesis of Mn-doped cesium lead halide quantum dots with high Mn substitution ratio. *J. Phys. Chem. Lett.* **2017**, *8*, 4167–4171. [CrossRef]
30. Guria, A.K.; Dutta, S.K.; Adhikari, S.D.; Pradhan, N. Doping Mn^{2+} in lead halide perovskite nanocrystals: Successes and challenges. *ACS Energy Lett.* **2017**, *2*, 1014–1021. [CrossRef]
31. Van der Stam, W.; Geuchies, J.J.; Altantzis, T.; van den Bos, K.H.; Meeldijk, J.D.; Van Aert, S.; Bals, S.; Vanmaekelbergh, D.; de Mello Donega, C. Highly emissive divalent-ion-doped colloidal $CsPb_{1-x}M_xBr_3$ perovskite nanocrystals through cation exchange. *J. Am. Chem. Soc.* **2017**, *139*, 4087–4097. [CrossRef] [PubMed]
32. Huang, G.; Wang, C.; Xu, S.; Zong, S.; Lu, J.; Wang, Z.; Lu, C.; Cui, Y. Postsynthetic doping of $MnCl_2$ molecules into preformed $CsPbBr_3$ perovskite nanocrystals via a halide exchange-driven cation exchange. *Adv. Mater.* **2017**, *29*, 1700095. [CrossRef] [PubMed]
33. Gao, D.; Qiao, B.; Xu, Z.; Song, D.; Song, P.; Liang, Z.; Shen, Z.; Cao, J.; Zhang, J.; Zhao, S. Postsynthetic, Reversible Cation Exchange between Pb^{2+} and Mn^{2+} in Cesium Lead Chloride Perovskite Nanocrystals. *J. Phys. Chem. C* **2017**, *121*, 20387–20395. [CrossRef]
34. Li, F.; Xia, Z.; Gong, Y.; Gu, L.; Liu, Q. Optical properties of Mn^{2+} doped cesium lead halide perovskite nanocrystals via a cation-anion co-substitution exchange reaction. *J. Mater. Chem. C* **2017**, *5*, 9281–9287. [CrossRef]
35. Yang, Y.; Li, Q.; Liu, Y.; Cong, R.; Sun, Y.; Hou, J.; Ge, M.; Shi, J.; Zhang, F.; Zhao, G.; et al. Magenta-emitting cesium lead halide nanocrystals encapsulated in dimethicone for white light-emitting diodes. *ACS Appl. Nano Mater.* **2020**, *3*, 4886–4892. [CrossRef]
36. Xu, K.; Vickers, E.T.; Luo, B.; Allen, A.C.; Chen, E.; Roseman, G.; Wang, Q.; Kliger, D.S.; Millhauser, G.L.; Yang, W.; et al. First synthesis of Mn-doped cesium lead bromide perovskite magic sized clusters at room temperature. *J. Phys. Chem. Lett.* **2020**, *11*, 1162–1169. [CrossRef]
37. Almutlaq, J.; Mir, W.J.; Gutiérrez-Arzaluz, L.; Yin, J.; Vasylevskyi, S.; Maity, P.; Liu, J.; Naphade, R.; Mohammed, O.F.; Bakr, O.M. $CsMnBr_3$: Lead-Free Nanocrystals with High Photoluminescence Quantum Yield and Picosecond Radiative Lifetime. *ACS Materials Lett.* **2021**, *3*, 290–297. [CrossRef]
38. De, A.; Mondal, N.; Samanta, A. Luminescence tuning and exciton dynamics of Mn-doped $CsPbCl_3$ nanocrystals. *Nanoscale* **2017**, *9*, 16722–16727. [CrossRef] [PubMed]
39. Hills-Kimball, K.; Pérez, M.J.; Nagaoka, Y.; Cai, T.; Yang, H.; Davis, A.H.; Zheng, W.; Chen, O. Ligand engineering for Mn^{2+} doping control in $CsPbCl_3$ perovskite nanocrystals via a quasi-solid–solid cation exchange reaction. *Chem. Mater.* **2020**, *32*, 2489–2500. [CrossRef]
40. Li, X.; Cai, W.; Guan, H.; Zhao, S.; Cao, S.; Chen, C.; Liu, M.; Zang, Z. Highly stable CsPbBr3 quantum dots by silica-coating and ligand modification for white light-emitting diodes and visible light communication. *Chem. Eng. J.* **2021**, *419*, 129551. [CrossRef]
41. Chen, W.; Shi, T.; Du, J.; Zang, Z.; Yao, Z.; Li, M.; Sun, K.; Hu, W.; Leng, Y.; Tang, X. Highly Stable Silica-Wrapped Mn-Doped $CsPbCl_3$ Quantum Dots for Bright White Light-Emitting Devices. *ACS Appl. Mater. Interfaces* **2018**, *10*, 43978–43986. [CrossRef]